Network-Based Ionospheric Gradient Monitoring to Support GBAS

Maria Caamano[1,2], Michael Felux[1], Daniel Gerbeth[1], Jose Miguel Juan[2], Guillermo Gonzalez-Casado[2] and Jaume Sanz[2]

[1]*German Aerospace Center (DLR)*
[2]*Research Group of Astronomy and Geomatics, Polytechnic University of Catalonia*

BIOGRAPHIES

Maria Caamano is a research engineer at the German Aerospace Center (DLR). Since September 2017, she is doing her Ph.D. as an external student of gAGE/UPC in the Doctoral Program in Aerospace Science and Technology (DOCTA). Her main research interests are the impact of ionospheric irregularities in the single-frequency single-constellation GBAS and the future development of multi-frequency multi-constellation GBAS.

Dr. Michael Felux is a research engineer at the German Aerospace Center (DLR). Since 2015 he is coordinating DLR's research on GBAS-based navigation. His main research interest is the total system performance of GBAS-based Automatic Landings.

Daniel Gerbeth is a research engineer at the German Aerospace Center (DLR). His current research interest focus on the implementation of mobile low-cost GBAS for UAV navigation.

Dr. Jose Miguel Juan is senior researcher at gAGE/UPC. His current research interests are in the area of GNSS data processing Algorithms for High Accuracy GNSS Navigation and GNSS ionospheric sounding, as well as Augmentation Systems (SBAS and GBAS).

Dr. Guillermo Gonzalez-Casado is senior researcher at gAGE/UPC. His current research interests are GNSS data processing and ionospheric sounding, high accuracy GNSS Navigation and Augmentation Systems (SBAS and GBAS).

Dr. Jaume Sanz is senior researcher at gAGE/UPC. His current research interests are in the area of GNSS data processing algorithms, GNSS ionospheric sounding, augmentation systems (SBAS and GBAS), and High Accuracy GNSS Navigation.

ABSTRACT

Ionospheric anomalies, like large ionospheric gradients, might produce a difference between the ionospheric error experienced by the Ground Based Augmentation System (GBAS) reference station and the aircraft on approach. This ionospheric delay difference could lead to hazardous position errors if undetected.
For that reason, the GBAS Approach Service Types (GAST) C and D provide solutions against this threat, but the methods employed still face challenges by limiting the availability in certain cases, especially in regions with severe ionospheric conditions. This issue is caused by the use of very conservative ionospheric threat models derived based on the worst-ever-experienced ionospheric gradients in the relevant region. However, these worst-case gradients occur very rarely.
Therefore, this paper proposes a methodology capable of detecting ionospheric gradients in real-time and estimating their parameters in near real-time by using a wide area network of dual-frequency and multi-constellation GNSS monitoring stations. Hence, the GBAS stations could use this information to update the threat model currently applied in their algorithms, which would result in an improvement of the GBAS availability in regions where it is degraded.
The detection and estimation algorithm is initially theoretically explained. Then, the performance of this algorithm is evaluated with simulated gradients and with a real gradient, utilizing for both the real measurements recorded by a reference network in Alaska. The synthetic gradients are simulated over the nominal real measurements from this network and all the gradient parameters are modified within their ranges in the already existing threat models. In this way, we assess the performance of our algorithm by comparing the differences between the known simulated gradient parameters and the parameters estimated by our algorithm. Additionally, we also evaluate our algorithm with one real ionospheric gradient measured by the same network in Alaska to study the differences between using simulated gradients and real gradients.

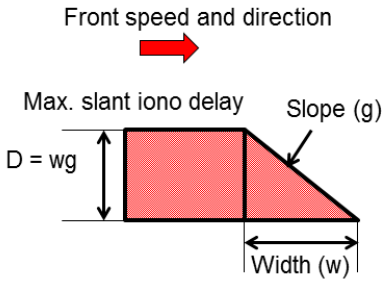

PARAMETER	CONUS	GERMANY	BRASIL
Max. front slope (g) [mm/km]	425	140	860
Front width (w) [km]	25 - 200	20 - 200	22 - 454
Front speed (v) [m/s]	0 - 750	0 - 1200	40 - 246
Front direction (d) [°]	0 - 360	0 - 360	Within tilt angle of mag. equator
Max. differential delay (D) [m]	50	50	35

Figure 1: Ionospheric gradient threat model in GBAS and gradient parameters.

Results with both simulated gradients and the real gradient show the potential of our methodology to support GBAS stations by detecting and estimating the ionospheric gradients instead of using worst case models all the time.

I. INTRODUCTION

The Ground Based Augmentation System (GBAS) is a local-area, airport-based augmentation of Global Navigation Satellite Systems (GNSSs). Its main purpose is to enhance GNSS performance in terms of integrity, continuity, accuracy and availability. A GBAS reference station broadcasts differential corrections along with integrity parameters. The differential corrections enable the aircraft approaching the airport to correct the navigation signals from the satellites by removing the spatially correlated errors between the ground station and the aircraft. Thus, the aircraft is able to improve the accuracy of its position estimation. Additionally, the integrity parameters enable the airborne system to calculate bounds of the residual position errors and ensure the safety of the operation.

Single-frequency (L1) single-constellation (GPS) differential corrections, as they are provided today by the GBAS ground station, enable the airborne users to correct most of the GPS ranging errors, especially the ones caused by the experienced ionospheric delay. However, ionospheric anomalies, like large ionospheric gradients, might produce a difference between the ionospheric error experienced by the GBAS reference station and the aircraft on approach. This ionospheric delay difference could lead to hazardous position errors if undetected, since it is not correctly overbounded by the integrity parameters and therefore results in misleading integrity information. For that reason, the GBAS Approach Service Types (GAST) C [1] and D [2] provide solutions to mitigate the ionospheric gradient threat, but the methods employed still face challenges by limiting availability in certain cases.

A GAST-C ground station, developed to support CAT-I operations, inflates the integrity parameters in order to exclude potentially usable satellite geometries that could produce unacceptably large position errors if affected by a worst case gradient. This worst case gradient is modelled as a wave front of a certain magnitude (represented by the slope and width) moving with constant speed and direction (Figure 1). Furthermore, the worst case gradient belongs to a threat model that is derived based on the worst-ever-experienced ionospheric gradients measured in the relevant region and defines a range of values for the gradient parameters that combined could harm GBAS. In Figure 1, we show the threat model and its main parameters for the CONUS region [3], Germany [4] and Brazil [5]. However, the main problem is that this methodology assumes that the worst case gradient is always present, while this is very unlikely. This strong assumption together with the high values of the threat model in regions with severe ionospheric conditions like Brazil can cause that satellite geometries are excluded even in days where no perturbation is present, leading to a loss of availability [6]. Moreover, the threat model is derived based on historical data and thus, this procedure cannot protect users against a larger gradient that might occur at some point in time in the future.

The GAST-D concept, developed to support CAT-II/III operations, contains a significant amount of monitors to cover all different regions of the mid-latitudes ionospheric threat model [7]. The main problem in this case is that the monitoring thresholds are very sensitive to false alarms because the assumption of an always present ionospheric gradient is still applied (prior probability of occurance of an ionospheric gradient of one). Moreover, one of the monitors designed to protect GAST D against ionospheric gradients (the Ionospheric Gradient Monitor, IGM [8]) has associated some siting constraints of the GBAS receivers because it has to cover a certain region of the ionospheric threat model, which makes also difficult its deployment in certain airports. While trying to adapt the GAST D concept to other regions with more severe ionospheric conditions, the previously mentioned issues could have a negative impact on GBAS availability [9].

In previous work [10], we proposed a real-time ionospheric monitoring approach that could reduce the conservative assumptions currently applied in GAST C and D and thus improve their availability under active ionospheric conditions. Moreover, we described how the monitor could work under nominal conditions and evaluated the impact of noise and multipath on the monitoring concept.

In this paper, we build on [10] to propose an algorithm that addresses the detection of ionospheric gradients in real-time and estimation of gradient parameters in near real-time. Furthermore, we evaluate our algorithm with simulated ionospheric gradients,

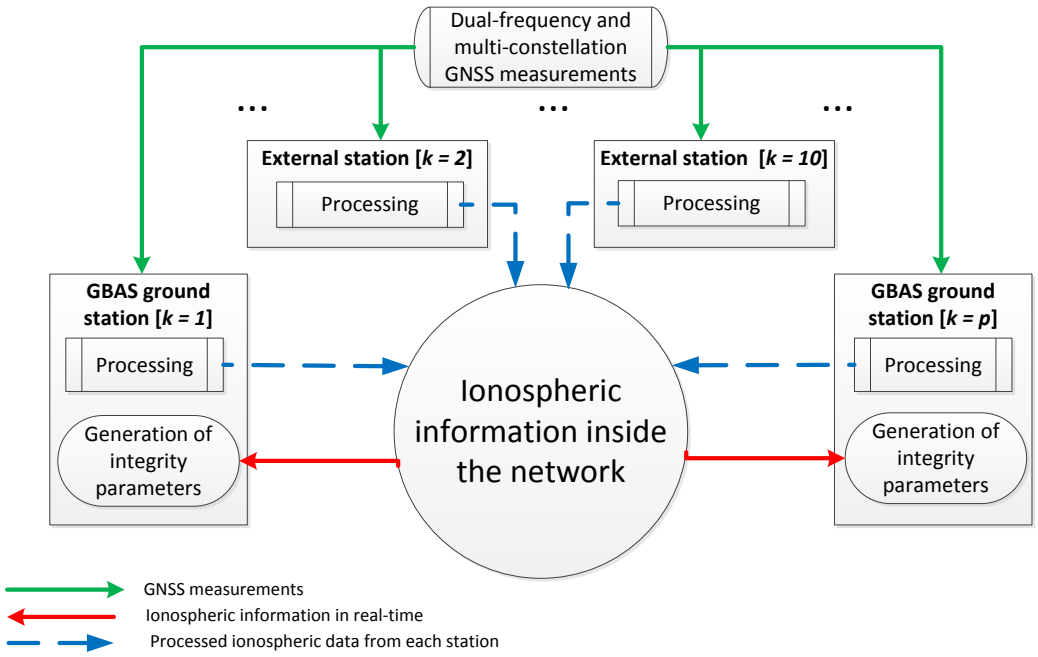

Figure 2: Simplified diagram of the network.

assessing the differences between the known simulated gradient parameters and the parameters estimated by our algorithm. These simulations correspond to regional/global ionospheric disturbances (i.e. beyond the GBAS local scale), which are based on actual perturbations. Additionally, we also evaluate our algorithm with a real ionospheric gradient measured by monitoring stations in Alaska to show the differences between using simulated gradients and real gradients.

This paper is divided into four main sections: Section II. reviews the real-time ionospheric monitoring concept, Section III. describes our algorithm for detection of the gradients and estimation of the gradient parameters, Section IV. introduces the simulation setup and the ionospheric gradient simulator and Section V. presents the results of the evaluation of the monitor with simulated gradients and a real gradient observed by a reference network.

II. DUAL FREQUENCY MONITORING CONCEPT

The availability of GBAS could be degraded due to many safe satellite geometries excluded by the ground station in GAST C and a high rate of false alarms in GAST D. The exclusion of safe satellite geometries occurs because the ground station assumes a worst-case gradient always present while this is extremely unlikely. The rate of false alarms, higher than desired, is problematic in GAST D while applying the same monitoring thresholds derived for mid-latitudes to regions in which the active ionosphere is not well represented with the mid-latitude ionospheric threat model [7].

For that reason, in [10], we proposed a real-time ionospheric monitoring concept that includes external information about the state of the ionosphere in GBAS instead of always relying on worst case models.

Our proposed monitor provides protection to all GBAS users by using a wide area network of dual-frequency and multi-constellation GNSS stations situated in carefully surveyed locations. The network would consist of mainly the GBAS stations installed in the relevant region that would need dual-frequency capable receivers or have a second dual-frequency receiver installed for monitoring purposes only. Since it is foreseen that the GBAS stations will be installed principally at important airports, the network would need other external monitoring stations that would enhance the coverage of the GBAS stations while monitoring for gradients.The dual-frequency measurements coming from both types of stations would be used to estimate the ionospheric delay reliably and therefore, for detecting ionospheric anomalies in real-time. Furthermore, the utilization of multiple constellations would provide an improved sampling of the ionospheric events and support also the single-frequency and single-constellation GBAS service types C and D by extending their knowledge of the ionospheric state. A GAST-C user could use this information instead of assuming the presence of a worst-case gradient while a GAST-D user could benefit from prior probabilities of occurrence of the gradient.

The functionality of the proposed monitoring network, depicted in Figure 2, is described in the following:

1. The processing part of each of the stations receives GNSS dual-frequency and multi-constellation code and carrier phase measurements and calculates the slant ionospheric delay as in Equation 1 [11]:

$$\widehat{I}^{j}_{f_1,k} = \frac{{f_2}^2}{{f_1}^2 - {f_2}^2}\left(\Phi^{j}_{f_1,k} - \Phi^{j}_{f_2,k}\right) \tag{1}$$

where $\Phi^{j}_{f_1,k}$ is the carrier phase measurement in meters for frequency f_1 (L1/E1) and $\Phi^{j}_{f_2,k}$ the carrier phase measurement in meters for frequency f_2 (L5/E5a). j represents a single satellite from the GPS or Galileo constellation and k the station that calculates the ionospheric delay. In the following, we denote as J the set of all the satellites in view and j a single satellite that can take the values $j = 1, 2, ..., n$, being n the total amount of satellites in view. In the same way, we denote as K the set of all the stations utilized for the calculations and k a single station that can take the values $k = 1, 2, ..., p$, being p the total amount of stations available. Moveover, note that the slant ionospheric delay is calculated in the so-called Ionospheric Pierce Points (IPPs), the points of intersection between the satellite-receiver line of sight and the ionosphere modelled as a "thin shell" located at 350 km above the Earth's surface [12].

2. The rate of change of the estimated ionospheric delay from each satellite j is compared with a predefined threshold derived with real measurements from this station k and integrity requirements. This threshold decides whether the ionosphere is calm or there is a perturbance in real-time. In Section III., we give more details about the threshold derivation and the detection algorithm.

3. The detection information from each of the stations per satellite is shared in the network in real-time. Then, a central processing estimates the nominal ionospheric parameters when it has not detected a gradient or the ionospheric gradient parameters when it has detected a perturbance. This gradient parameter estimation process is done per satellite and it needs that at least 3 stations have detected the gradient.

4. Each GBAS station is then responsible of using the network information to support the already existing equipment in covering the GBAS approaches of each airport. The minimum detectable gradient is calculated for every GBAS station taking into account the multipath and noise conditions, the location of the GBAS station and the network information for this location. Note that the GBAS stations situated on the borders of the monitoring network would not benefit directly from the estimation of the gradient parameters, since we need at least 3 stations to calculate them, but they could still benefit from the real-time detection capability of the network.

III. METHODS

With the aim of monitoring for possible gradients, we developed an algorithm that is able to detect the ionospheric gradients in real-time and estimate the gradient parameters like slope, width, speed and direction in near real-time. However, before the real-time operation of the algorithm, a pre-processing part is needed in order to derive the detection thresholds taking into account the characteristics of each of the stations in the monitoring network. In the following, we explain both parts: the derivation of the monitoring thresholds and the real-time operation of the algorithm.

A. Derivation of the monitoring thresholds

A correct monitoring threshold derivation is the key part in the algorithmic chain since it decides whether we measure an ionospheric gradient or not. Therefore, it is important to study the expected performance of each of the monitoring stations inside the network in days when no abnormal ionospheric activity was found. For that purpose, we select manually for each of the monitoring stations at least one day of dual-frequency and multi-constellation GNSS measurements recorded in nominal ionospheric conditions based on other ionospheric indices such as the AATR [13]. Nevertheless, even in nominal conditions, the carrier phase measurements might contain cycle slips that could result in false gradient detections and thus it is necessary to clean the data before calculating the threshold.
This data cleaning process consists of the following two stages:

1. A cycle slip detector explained in [14] and [15] searches for large jumps in the ionospheric delay computed as in Equation 1. However, after this process, some less evident cycle slips could remain undetected inside the calculated ionospheric delay and therefore rise the value of the computed thresholds degrading the detection performance of the monitoring network.

2. For this reason, a second cycle slip detector is applied to remove the possible remaining cycle slips. This second cycle slip detector calculates the ionospheric-free combination of the dual-frequency carrier phases, using precise orbit and clock corrections [15]. These values are completely independent of the ionospheric effects and usually below 10 cm, although they can grow larger for low elevation satellites. This high accuracy can be achieved thanks to the knowlegment of the precise coordinates of the receivers. Moreover, in order to automate the cycle slip detection and cleaning process, we define an acceptance level for the value of the ionospheric free-combination of the carrier phases. After studying the distribution of these values, we assume that the ionospheric-free combination of the carrier phase measurements can be approximated as a

Gaussian distribution with zero mean and a standard deviation (σ) that represents noise and multipath, and precise orbit and clock correction errors. We define an acceptance level of 3 over the standard deviation of this distribution calculated with the nominal data to be representative of its nominal behaviour based on our studies with real measurements. In Figure 3, we show an example of this acceptance level (in red) calculated for the data samples of the ionospheric-free combination of the carrier phases (in blue) computed for all the GPS satellites for the day 73 of year 2015 (calm day) and av16 station in Alaska (data available at https://www.unavco.org). Note that, due to the limited availability of data recorded with L1/L5 frequencies and Galileo constellation during active ionospheric conditions, we use for our tests with real measurements L1 and L2 frequencies and only the GPS constellation. The performance with L1/E1 and L5/E5a and GPS and Galileo is expected to be better due to the less noise of the L5/E5a frequency and the higher amount of information that more satellites add.

Comparing for each epoch the ionospheric-free combination value for each satellite with its predefined acceptance level, we can clean the ionospheric delay values from cycle slips corresponding to the same epoch.

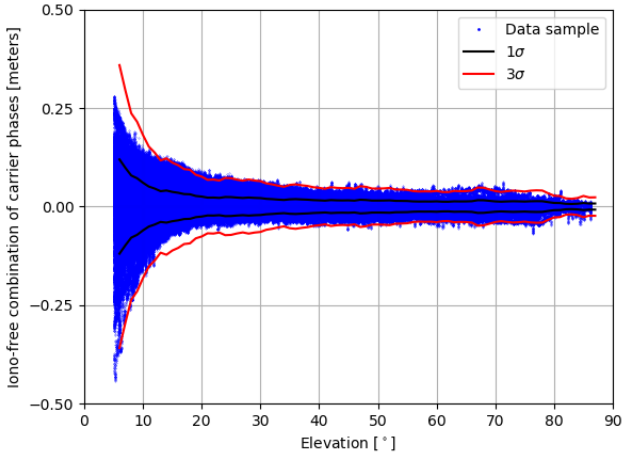

Figure 3: Acceptance level of the ionospheric-free combination of carrier phases for all satellites in view during day 73, year 2015, station av16 (Alaska).

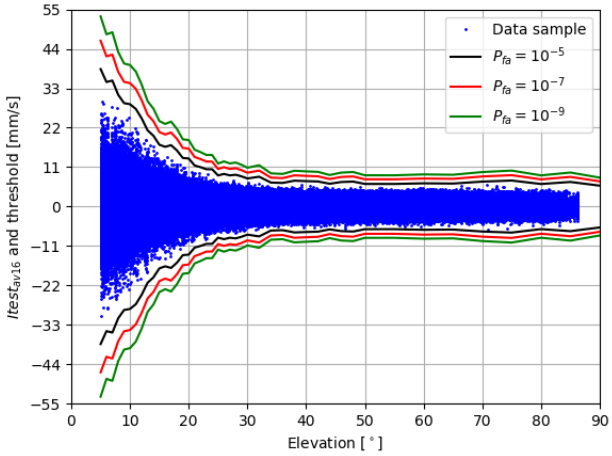

Figure 4: Test statistic values for all satellites in view and different thresholds during day 73, year 2015, station av16 (Alaska) .

Next, we derive the detection threshold for each of the monitoring stations k. First, we compute the test statistic, $Itest_k^j(t)$, for each epoch t, each satellite j and each station k as the first derivative or rate of the cleaned ionospheric delay in order to remove the unresolved ambiguities of the carrier phase measurements.

$$Itest_k^j(t) = \frac{\widehat{I}_{f_1,k}^j(t) - \widehat{I}_{f_1,k}^j(t-\delta_t)}{\delta_t} \tag{2}$$

Here, $\widehat{I}_{f_1,k}^j(t)$ is the ionospheric delay estimation for station k, satellite j and epoch t, $\widehat{I}_{f_1,k}^j(t-\delta_t)$ is ionospheric delay estimation for station k, satellite j and the previous epoch and δ_t is the time difference between two consecutive epochs. Note that any cycle slip would produce a high rate value if it is not detected and removed from the slant ionospheric delay estimation.
After that, we order these $Itest_k^j(t)$ computed for all the satellites J, all the epochs t during at least one day and one of the stations k in elevation bins. The size of these elevation bins depends also on the elevation: 1° between 5° and 30° of elevation, 2° between 30° and 50° of elevation and 5° between 50° and 90° of elevation. This different binning size is used to account for the less amount of samples available from high elevation satellites. Then, given an acceptable false alarm probability, P_{fa} a threshold for each station can be defined as:

$$T_k = k_{fa} \cdot \sigma_{Itest_k^J}(\theta) \tag{3}$$

where k_{fa} is the false alarm multiplier computed from the inverse of the standard normal cumulative distribution, $Q^{-1}\left(\frac{P_{fa}}{2}\right)$, and $\sigma_{Itest_k^J}$ is the standard deviation of the $Itest_k^J$ distribution for all the epochs and satellites for station k ordered in elevation bins with θ representing the elevation bins.
However, this methodology only applies if the $Itest_k^J$ distribution is Gaussian. In the case the probability distribution computed with the $Itest_k^J$ per bin presents a non Gaussian behaviour, we calculate a Gaussian overbound of the tails of the $Itest_k^J$ distribution per bin following the approach in [16], [17]. Therefore, the detection threshold for station k is defined as:

$$T_k = k_{fa} \cdot \sigma_{overbound\_Itest_k^J}(\theta) \tag{4}$$

with $\sigma_{overbound\_Itest_k^J}$ as the standard deviation of the Gaussian distribution that overbounds the tails of the probability distribution calculated with $Itest_k^J$. As stated in [17], in this case, the probability that a certain $Itest_k^j$ exceeds the threshold is smaller than the P_{fa} utilized to calculate the k_{fa} multiplier, which means that the requirement of false alarm probability of the monitor is satisfied. In the following, when we refer to a test statistic calculated for all the satellites we omit the J superscript and when we refer to all the epochs considered we omit the time indicator t.
In Figure 4, we show an example of different test statistic values (in blue) for all the satellites in view ($Itest_{av16}$) computed with the nominal data of day 73, year 2015 and station av16 (Alaska) and different values for the detection threshold depending on the different probabilites of false alarm considered. Here, we can observe that the $Itest_{av16}$ values in millimiters per second depend remarkably on the elevation due to the higher effects of the noise and multipath and therefore the threshold also gets larger for low elevation satellites. Concerning the different probabilites of false alarm, when we allow a larger amount of false alarms the threshold gets more restrictive and when we allow less false alarms the threshold is relaxed, but then some gradients could be missed. Therefore, we selected a P_{fa} of 10^{-7} and an elevation mask of 10° as an acceptable compromise for our tests with real measurements.

B. Real-time operation of the algorithm

The real-time operation of the algorithm can also be divided into two main parts: the detection step and the estimation step.

Detection step

As previously stated in Section II., the detection step is performed individually per station k, satellite j and epoch t, monitoring for ionospheric anomalies in the rate of the slant ionospheric delay estimations.
The detection algorithm receives the GNSS dual-frequency and multi-constellation carrier phase measurements and calculates the slant ionospheric delay as in Equation 1. Then, these measurements undergo exactly the same cleaning process as in Section A. That is, the removal of the cycle slips by applying two successive cycle slip detectors, using for the second cycle slip detector in real-time the acceptance level predefined with nominal data. Once the data is clean, we compute the test statistic $Itest_k^j(t)$ (Equation 2).
Given a predefined threshold for a certain monitoring station k and considering its value for the elevation of a satellite j at a certain epoch t, $\theta_k^j(t)$, the condition for detecting the ionospheric gradients is:

$$\left|Itest_k^j(t)\right| \geq T_k\left(\theta_k^j(t)\right) \tag{5}$$

In Figures 5 and 6, we show an example of several ionospheric gradients for GPS satellite 3 and station av16 that were detected by our algorithm. Figure 5 shows the slant ionospheric delay values calculated with Equation 1. Since the ambiguities of the carrier phase measurements remain unresolved, we notice a negative shift of the ionospheric delay values, but this does not affect the value of its rate if we control that no cycle slip was undetected preventing false alarms. Figure 6 is a zoom of the $Itest_{av16}^3$ calculated for the slant ionospheric delays between 62340 and 62520 GPS seconds of day (area inside the black rectangle in Figure 5). The largest gradient (area inside the green rectangle) corresponds to the ascendent ramp in the ionospheric delay values depicted in Figure 5 and it is the gradient that we choose for the study with the real measurements in Section V.

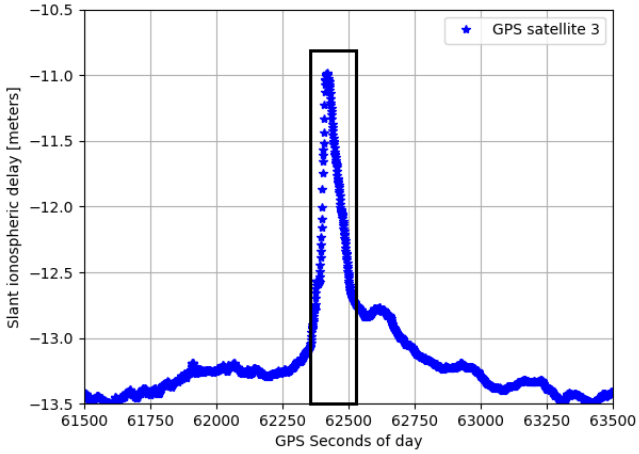

Figure 5: Slant ionospheric delay values during an ionospheric gradient occurance for GPS satellite 3 of day 76, year 2015, station av16 (Alaska).

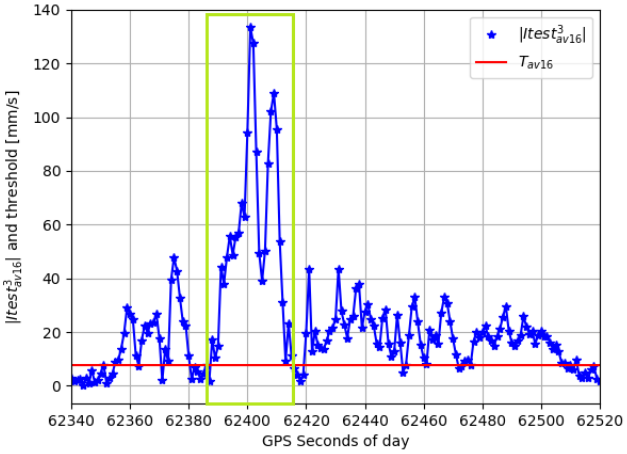

Figure 6: Absolute value of the test statistic and threshold for GPS satellite 3 of day 76, year 2015, station av16 (Alaska).

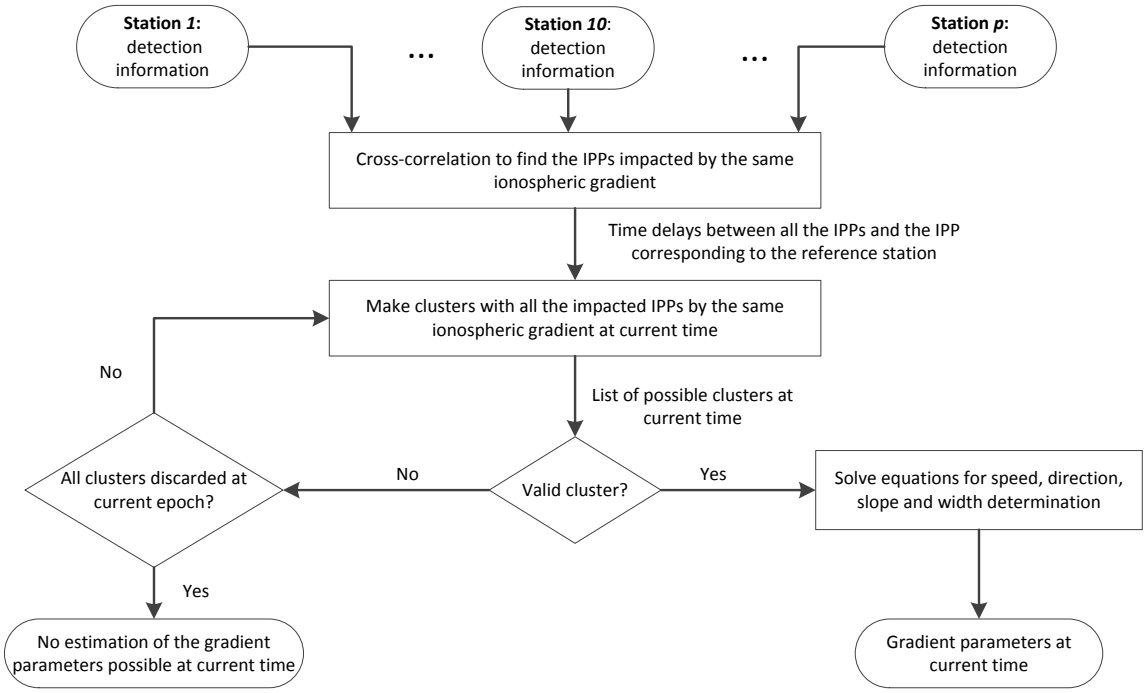

Figure 7: Flow chart of estimation algorithm.

Finally, the detection information is shared in the network of monitoring stations for all the IPPs (belonging to each satellite and each station) in real-time. This detection information consist of:

- $Itest_k^j(t)$: the test statistic for all stations K, satellites J and epoch t.
- $detection\_flag_k^j(t)$: contains ones associated with the times where the absolute value of the test statistic exceeded the threshold and zero otherwise.
- $signal\_flag_k^j(t)$: contains ones when there is a value of $Itest_k^j(t)$ for epoch t and zero when there is no signal or we detected a cycle slip.

Estimation step

The estimation step of the algorithm collects the detection information shared in the network per satellite in real-time and estimates the gradient parameters explained in Section I.: speed, direction, slope and width of the gradient. All the formulas in the following are expressed therefore for a single satellite j. A summarized flow chart for the estimation of the gradient parameters is shown in Figure 7.

Speed and direction of the gradient

In order to calculate the speed of the ionospheric gradient, we need to track its spatial evolution with time or, in other words, the time delay Δt_k^j between detections in two stations that are separated apart, a station k and a station that we choose as reference. We select as reference station the first station that detects the gradient. Additionally, we assume that the ionospheric perturbance is local, maintaining its characteristics of magnitude (slope and width) and propagation (speed and direction) constant for a certain period of time. Furthermore, we also consider that the ionospheric disturbance propagates as a planar wave (Figure 8) that moves with a speed $\vec{v}$ and impacts the different IPP_k^j corresponding to the same satellite j and different stations $k = 1, 2, ..., p$ at different times.

However, since in each ground station several ionospheric gradients can occur in a short period of time (as we can see in Figures 5 and 6), it is necessary to identify the same gradient occuring at different ground stations. Under the assumption that the gradient maintains its characteristics of magnitude during a certain period of time, this means that we need to identify the gradient with the same shape in different stations. To this end, we compute the cross-correlation between the test statistic values, calculated in different stations for the same satellite. Nevertheless, due to the real-time costraint in GBAS, it is necessary to perform the cross-correlation between the test statistics as fast as possible instead of using the complete set of measurements for a day. Thus,

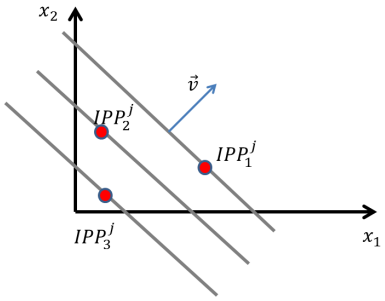

Figure 8: Planar wave propagation with speed $\vec{v}$.

we calculate the cross-correlation between buffers containing a history of test statistic values. We describe this procedure in the following taking as example two stations $k = 1,2$, assuming $k = 1$ as the reference:

1. We initialize the buffers of data as empty ($B\_Itest_1^j$ = [] and $B\_Itest_2^j$ = []).
2. For each epoch, t, the $Itest_1^j(t)$ and $Itest_2^j(t)$ values are stored in their respective buffers of data. If at some epoch we lose the signal or there was a cycle slip for any of the stations k ($signal\_flag_k^j(t)$ equals to 1), the buffer of data for this station is reset to empty.
3. In the moment the $detection\_flag_k^j(t)$ is equal to 1 for both of the stations and while $signal\_flag_k^j(t)$ is still 1, we begin to compute the cross-correlation between the two buffers $B\_Itest_1^j$ and $B\_Itest_2^j$. When the result of the cross-correlation is over the 95%, we calculate the time delay Δt_2^j of station $k = 2$ with respect to the reference station $k = 1$.
4. Once we found the time delay between the two stations, we consider it to be constant during the propagation of the gradient until we find another maximum of the cross-correlation over the 95%. In this case, we update the time delay Δt_2^j with the new result.
5. We continue to compute the cross-correlation between the two buffers until the $detection\_flag_k^j(t)$ is 0 for both of the stations, which means that the actual gradient is over for both stations. Therefore, we reset the buffers to empty again until we detect a new gradient. As an example, a single gradient in Figure 6 is considered between 62385 and 62417 GPS seconds of day (green rectangle).

Once we identified the same ionospheric perturbation detected in at least 3 stations and calculated the time delays between the stations and the station of reference ($k = 1$ in the example), we can already estimate the speed vector of the gradient, $\vec{v}$. However, as previously stated, we assume that the perturbation is local, which means that the result of comparing the measurements from two stations with a long distance between them (e.g. 300 km) might be innacurate since the perturbation might change completely during its propagation from one station to the next. Moreover, the geometry of the IPPs in the sky should not be aligned in order to avoid singularities while calculating the speed vector.
Therefore, before the estimation of the gradient parameters, we group the IPPs corresponding to the different stations in clusters and we validate these clusters to check if they are suitable to calculate a reliable estimation of the speed vector. At each epoch t, we compute the position vectors $\vec{x}_k^j(t)$ for each of the IPPs corresponding to satellite j and different stations $k = 1,2,...,p$ impacted by the same gradient in a local coordinate system. Then, we form a cluster with these position vectors, which is validated attending to two different criteria: i) a radius around the central point of the local coordinate system to guarantee the locality principle and ii) a geometry index that ensures that the geometry of the IPPs in the sky is acceptable. We define the geometry index (GI) as:

$$GI = \sqrt{GGI(1,1) + GGI(2,2)} \tag{6}$$

where $GGI(1,1)$ and $GGI(2,2)$ are elements of the general geometry index matrix calculated as:

$$GGI = \left[A^T A\right]^{-1} \tag{7}$$

and A is:

$$A = \begin{bmatrix} \frac{x_{11}^j}{d_1^j} & \frac{x_{21}^j}{d_1^j} & -1 \\ \frac{x_{12}^j}{d_2^j} & \frac{x_{22}^j}{d_2^j} & -1 \\ \vdots & \vdots & \vdots \\ \frac{x_{1p}^j}{d_p^j} & \frac{x_{2p}^j}{d_p^j} & -1 \end{bmatrix} \tag{8}$$

Here, $x_{1_p}^j$ is the East coordinate of the IPP in the local coordinate system for station $k = p$, $x_{2_p}^j$ is the North coordinate in the local coordinate system for station $k = p$ and d_p^j is the great circle distance between the center point of the local coordinate system and the IPP_p^j.
After validating the clusters, we first estimate the speed vector, its module and its direction. For this purpose, we apply the work accomplished in [4] and [18]. Under the assumption that the ionospheric disturbance propagates as a planar wave, the planar wave phase ϕ can be expressed as:

$$\phi = \vec{k} \cdot \vec{x} - \omega t + \phi_0 \tag{9}$$

where $\vec{k}$ is the angular wave number vector, $\vec{x}$ is the position vector, ω is the angular frequency and ϕ_0 is the initial phase.
Giving an ionospheric perturbance affecting the observations of a certain GPS satellite j, the condition to obtain the same phase between the corresponding perturbation observed from two receivers of the network (for example $k = 1$ as reference and another $k = 2$), can be written as:

$$\vec{k} \cdot \left(\vec{x}_2^j - \vec{x}_1^j \right) = \omega \left(t_2^j - t_1^j \right) \tag{10}$$

where $\vec{x}_2^j$ is the position vector of the IPP_2^j in a local reference coodinate system, $\vec{x}_1^j$ is the position vector of the IPP_1^j taken as reference in the local reference coordiante system, t_2^j is the detection time in the station 2 and t_1^j is the detection time in the station 1. Defining the vector slowliness as $\vec{s} = \frac{\vec{k}}{\omega}$ as in [18] and expressing t_k^j in terms of the time delay:

$$\vec{s}^j \cdot \left(\vec{x}_2^j - \vec{x}_1^j \right) = \Delta t_2^j \tag{11}$$

Since the speed of the gradient and also the slowliness vector are estimated by different satellites, in the following we denote as $\vec{s}^j$ and $\vec{v}^j$ the estimation of these vectors by each of the satellites j. Then, the speed of the gradient $\vec{v}$ is the inverse of the vector $\vec{s}^j$:

$$\vec{v}^j = \frac{\vec{s}^j}{\vec{s}^j \cdot \vec{s}^j} \tag{12}$$

By solving the system of equations that results of substituting in Equation 11 the station $k = 2$ with the information of the IPPs corresponding to at least 3 impacted stations, we estimate the speed vector of the gradient, its module and its direction.

Slope and width of the gradient

When the speed vector of the gradient is known, the slant slope of the gradient estimated by satellite j and station k is determined by the following geometrical relationship:

$$g_k^j(t) = \frac{Itest_k^j(t)}{\Delta v_k^j(t)} \tag{13}$$

where Δv_k^j is the relative speed between the gradient and the IPP projected in the direction of propagation of the gradient calculated as:

$$\Delta v_k^j(t) = \left(\vec{v}_{IPP_k^j}(t) - \vec{v}^j(t) \right) \frac{\vec{v}^j(t)}{\| \vec{v}^j(t) \|} \tag{14}$$

The width of the gradient estimated by satellite j and station k is calculated as:

$$w_k^j(t) = \Delta v_k^j(t) \cdot T_W(t) \tag{15}$$

where T_W is the time in seconds that have passed since the gradient was detected ($detection\_flag_k^j$ equal to 1 and $signal\_flag_k^j$ equal to 1).
All the satellites affected by the gradient estimate the gradient parameters and provide the current state of the ionosphere in the monitored area. Then, it is the task of each of the GBAS ground stations to use this information to update the threat model to be used in a certain moment.

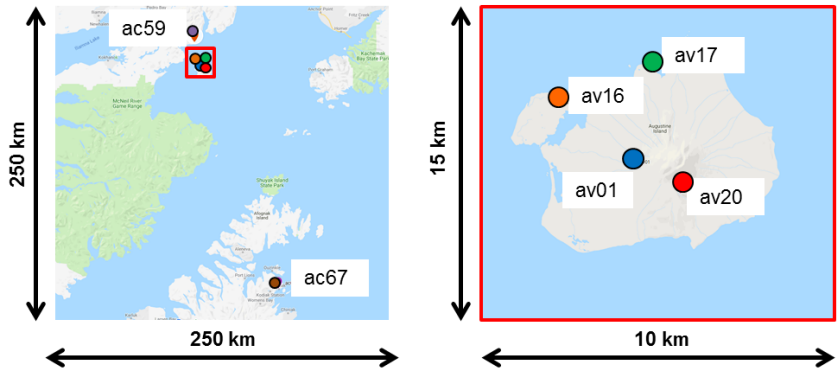

NAME	LAT [°]	LON [°]
av01	59.359	-153.461
av16	59.386	-153.535
av17	59.404	-153.451
av20	59.347	-153.428
ac59	59.567	-153.585
ac67	57.791	-152.425

Figure 9: Station coordinates.

IV. SIMULATION SETUP

In this section, we introduce the simulation setup that we use to evaluate the differences between the known simulated gradient parameters and the parameters estimated by our algorithm. The simulation setup consists of a real network of stations that already measured real ionospheric gradients and a synthetic ionospheric perturbance simulated to be representative of the GBAS threat model shown in Figure 1.

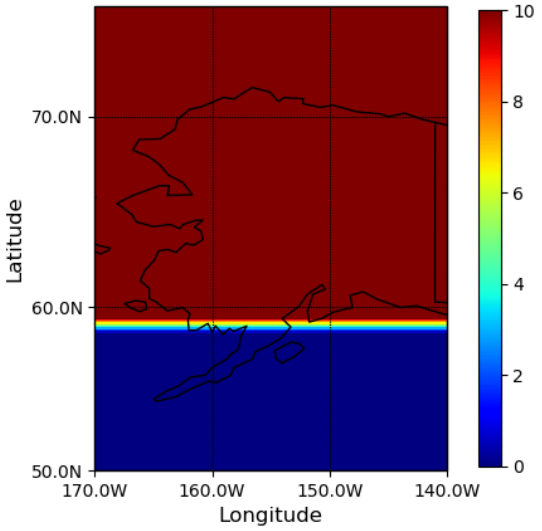

Figure 10: Vertical ionospheric delay in meters for one simulated gradient.

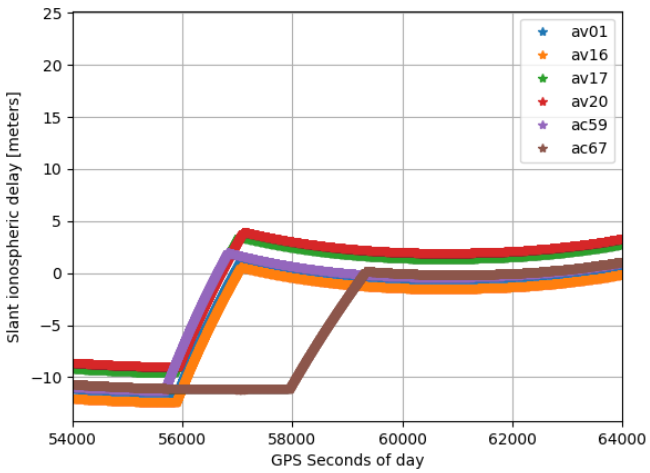

Figure 11: Slant ionospheric delay simulated for GPS satellite 1 over the nominal ionosphere on a calm day (73 year 2015, Alaska).

The selected network of stations for our study is situated in Alaska and depicted in Figure 9. Public data is available for this network at 1 Hz of sampling rate for L1 and L2 frequencies and GPS satellites (https://www.unavco.org). From all the data available, we choose one day with no ionospheric disturbances (calm day, 73 of year 2015) to derive the detection thresholds.

Then, we simulate the ionospheric gradients over the nominal slant ionospheric delay calculated with the carrier phase measurements (Equation 1) of the considered calm day (73 of year 2015). For that purpose, we define the synthetic perturbation as a planar front depicted in Figure 10. This figure shows an ionospheric gradient or change in the ionospheric delay values between the dark blue area and the dark red area, which are the areas where the ionospheric delay values are constant and no gradient is present. In this case, the ionospheric delay values are expressed in the vertical domain to be independent of the elevation of each of the satellites, which allows us to simulate the same ionospheric perturbance for all the satellites. These vertical ionospheric delays are simulated by the utilization of two different simulation gradient parameters: the vertical slope in milimeters per kilometer and the width in kilometers. In the case of Figure 10, these parameters are 100 mm/km for the vertical slope and 100 km for the total width of the gradient resulting in a maximum simulated vertical ionospheric delay of 10 meters. Therefore, when an IPP corresponding to a certain satellite and station moves into the region with the gradient, we compute the distance from the IPP to the point where the perturbation starts (line that separates the blue area from the multicolor area in Figure 10) in kilometers and we multiply it with the vertical slope to get the vertical ionospheric delay. This vertical delay is then translated into a slant delay by multipliying with an obliquity factor (see equation in [11]) that depends on the elevation of the satellite. Furthermore, this

ionospheric gradient moves with a constant speed (meters per second) and direction (degrees) over a "thin shell" layer at a height of 350 km above the Earth's surface.
For our studies, we vary all the already defined simulation gradient parameters within their ranges in the CONUS and German threat models up to a maximum differential delay of 50 meters. Specifically, we vary the vertical slope in order to get slant slopes between 25 and 425 mm/km, the width between 20 and 200 km, the speed between 0 and 1200 m/s and the direction between 0° and 360°. In Figure 11, an example of the slant ionospheric delay simulated for GPS satellite 1 and all the considered stations is presented. Here, we can observe that the values of the slant ionospheric delay resulting of adding the synthetic perturbation corresponding to Figure 10 to the existing nominal values are negative. The reason is that the nominal slant ionospheric delays have still the ambiguities unresolved, but as previously stated, this issue is solved when calculating the test statistic as the rate of the ionospheric delay.

V. RESULTS AND DISCUSSION

A. Detection and estimation results with simulated gradients

When ionospheric gradients are simulated, we observe differences in the estimation capabilities of the algorithm while considering different characteristics of the gradient. However, varying the slope, the width or the direction of the gradient within their simulation ranges described in Section IV., while mainting constant all the other simulation parameters, produces no substancial differences in the estimation errors as long as the gradient is detected during all the time it lasts.
In the case of the direction variation, this can be explained because we used always the stations *av*01, *av*16, *av*17, *av*20 and *ac*59 to estimate the gradient parameters. This network has the same performance when the gradient comes from all the different directions as long as the gradient is not detected in two stations at the same time, situation that we prevent by selecting a geometry index (*GI*) defined in Section III. of 3. This value of the GI is what we defined to be representative of a good distribution of the IPPs in the sky. The station *ac*67 is not used by the algorithm because it is isolated with respect to the other stations (see Figure 9) and the same perturbation is measured by the same satellite but with a different elevation. Thus, it is not recognized by the algorithm as the same perturbation as the one measured by all the other stations. This fact can be seen in the example of Figure 11, where the gradient represented by the brown curve is less steeper than for all the other curves. Moreover, if we lower the accepted value for the cross-correlation down to 85% and validate the clusters conformed by the IPPs from all the stations including *ac*67, the geometry indices calculated exceed the value of 3.
In the case of the slope and width variation, the estimation errors are also similar for the different values within their range as long as the simulated gradient is large enough to be detected. The detectability curve calculated after removing the effect of the movement of the IPPs is shown in Figure 12. As we can observe, for a P_{fa} of 10^{-7} and an elevation mask of 10° we are not able to detect gradients below 58 mm/km until the satellites are in middle elevations. This is due to the noise and multipath in the $Itest_k^j$ values. One example of this issue is depicted for GPS satellite 1 (elevation of 30°) and all the considered stations in Figure 13. As we can see, the $Itest_k^1$ values vary greatly due to the noise and multipath present in the carrier phase measurements, which becomes more important while computing the test statistic values every second.

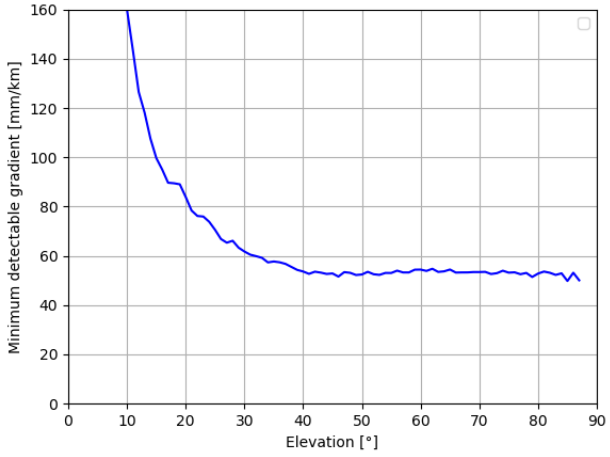

Figure 12: Worst-case minimum detectable gradient by all stations.

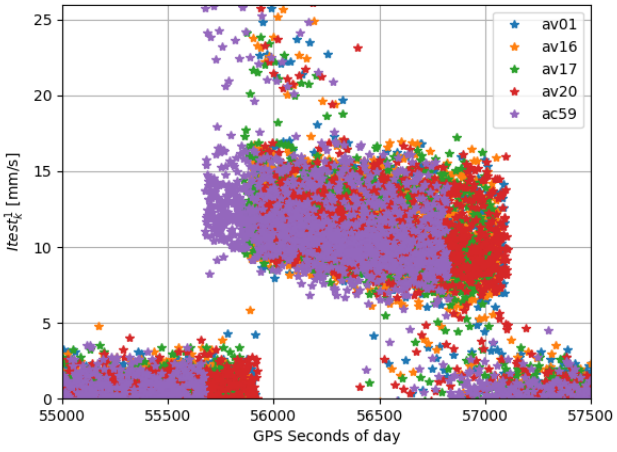

Figure 13: Example of simulation test statistic values for GPS satellite 1, day 73 of year 2015 (Alaska).

The variation of the simulated speed of the gradient is the only situation that produces noticeable impact on the estimation of the gradient parameters. Figures 14, 15, 16 and 17 show an example of the estimation errors of the different gradient parameters with the speed variation, when they have the following constant values: vertical slope is 150 mm/km, width is 100 km and direction is 180° (North to South). We also consider the estimation errors for three different situations: i) the gradient is the synthetic

perturbation only (without the nominal noise and multipath) measured by the GPS satellite 1 when it is at a low elevation, ii) the gradient is the synthetic perturbation simulated over the nominal measurements measured by the GPS satellite 1 when it is at the same low elevation and iii) the gradient is the synthetic perturbation simulated over the nominal measurements measured by the GPS satellite 1 when it is at a high elevation.

Figure 14 shows the speed estimation error while varying it between 0 and 1200 m/s. Here, we observe that the speed estimation errors for slow gradients are as large as approximately 17.5 m/s (17.5% of 100 m/s) in the case of the low elevation satellite with noise and multipath. However, the results with the same perturbation without noise and multipath (blue line) show a much smaller error. Therefore, we conclude that these errors are due to the poor performance of the cross-correlation when the test statistic values contain the effects of noise and multipath. When the satellite is at a high elevation, less error for low speed values is found in comparison with the situation when the satellite is at a low elevation because it contains less multipath and noise effects. When increasing the speed, the error in the speed estimation also increases (percentage from the simulated value) and both the red line and the blue line present a very similar behaviour. In this case, the estimation errors come from the geometrical approximations assumed to estimate the speed of the gradient in Section III. These assumptions together with and insufficient sampling rate causes the algorithm to be very sensitive to high speeds of the gradient because all the stations detect the gradients almost at the same times. We observe that the high elevation satellite presents also in this case large values for the speed estimation error (5% of 1050 m/s is 52.5 m/s).

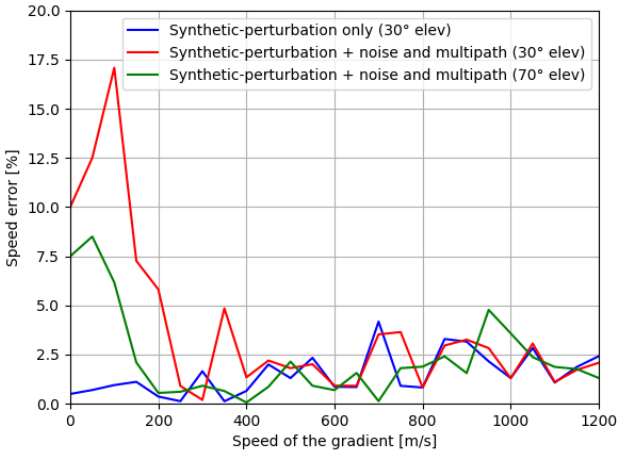

Figure 14: Speed errors for GPS satellite 1.

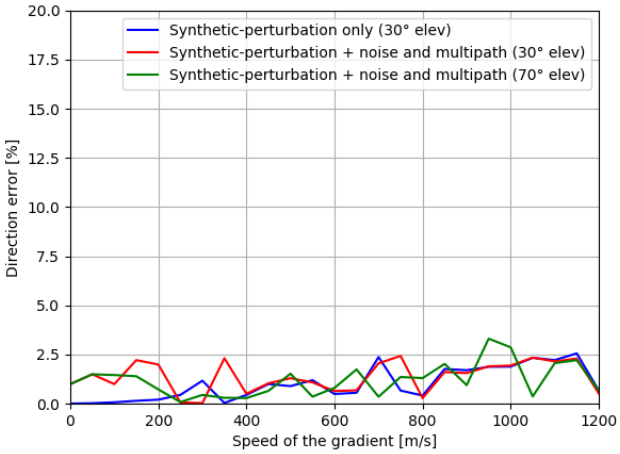

Figure 15: Direction errors for GPS satellite 1.

In the slope estimation error presented in Figure 16, we can also observe the effects of the noise and multipath when the gradient moves with speeds below 400 m/s. The reason here is that for lower speeds, the test statistic values are divided by smaller relative speeds between the IPPs and the gradient to calculate the slope (Equation 13) and therefore the noise and multipath effects get more critical. However, when the gradient moves with higher speeds, the effects of noise and multipath are smoothed out, and we observe again the errors depending on the geometrical approximations assumed.

Both the direction and width estimation errors depicted in Figures 15 and 17 present the same behaviour with the noise and multipath and the geometrical approximation errors, but in this case, these effects are less critical and therefore the calculation of these two parameters is more robust.

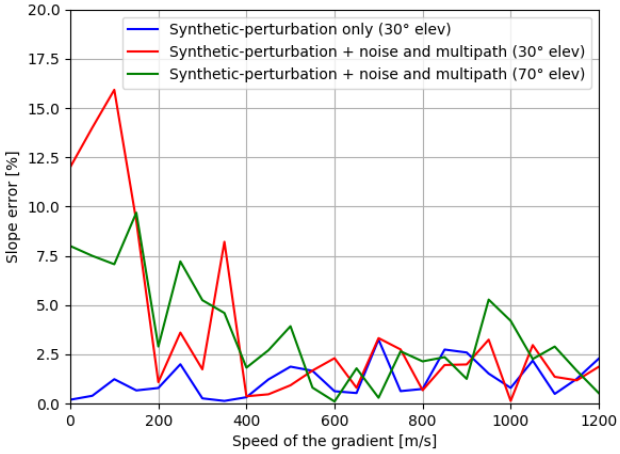

Figure 16: Slope errors for GPS satellite 1.

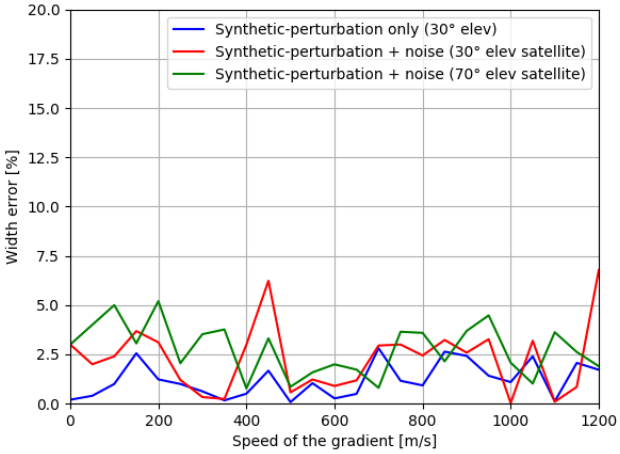

Figure 17: Width errors for GPS satellite 1.

B. Detection and estimation results with real gradients

Additionally, we also evaluate our algorithm with a real gradient measured by the network in Alaska (Figure 9) under active ionospheric conditions. The selected real gradient is the one depicted in Figures 5 and 6 measured by GPS satellite 3. After applying the thresholds derived as explained in Section III. and exemplified in Figure 6, we show the detected gradients in Figure 18 represented with solid lines. The detected gradients coincide with the steepest slopes in the slant ionospheric delays. Thus, we conclude that the gradients are adequately detected.

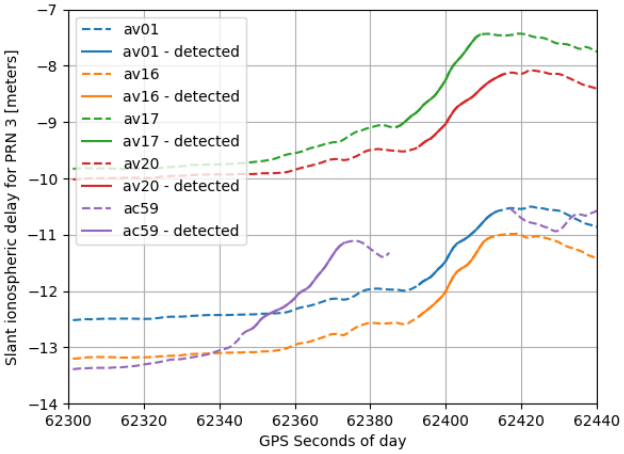

Figure 18: Slant ionospheric delay for the studied gradient (GPS satellite 3, day 76 of year 2015, Alaska).

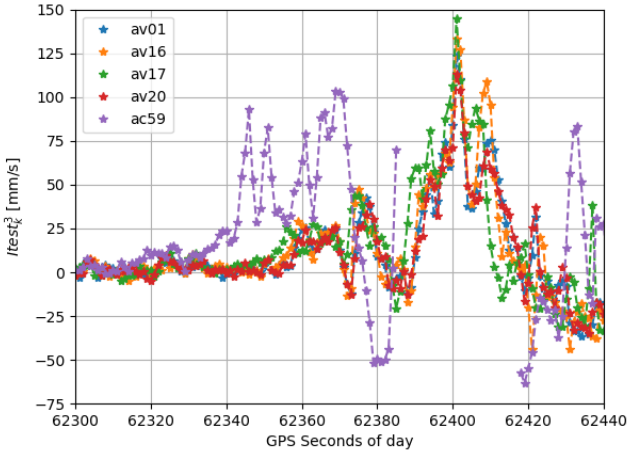

Figure 19: Test statistic of the studied gradient (GPS satellite 3, day 76 of year 2015, Alaska).

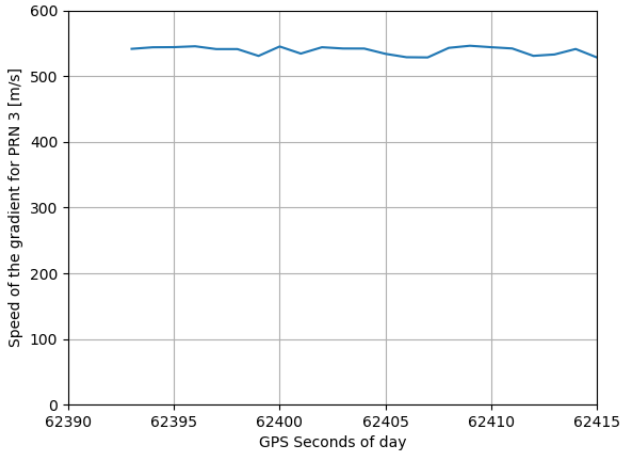

Figure 20: Speed of the gradient (GPS satellite 3, day 76 of year 2015, Alaska).

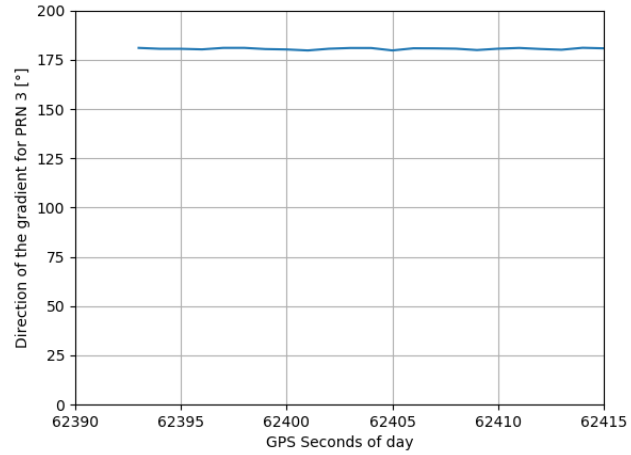

Figure 21: Direction of the gradient (GPS satellite 3, day 76 of year 2015, Alaska).

However, when we calculate the test statistic values, they are not sufficiently correlated between them to find the time delay between the stations (Figure 19). The reason is not the change of the elevation of the satellite as in the simulation results since the stations are 20 km apart. In this case, the perturbation has changed slightly with its propagation and this fact affects the shape of the first derivative calculated every second. One solution here would be not to consider station *ac*59 for the estimation of the gradient parameters and use only the others (*av*01, *av*16, *av*17 and *av*20). The problem is that these stations are extremely close to each other (around 5 km) and they detect the perturbation almost at the same time, making it impossible to calculate the gradient parameters with the methodology proposed.

Nevertheless, if we lower the cross-correlation value to be considered while calculating the time delays from 95% down to 85%, we find a correlation between all the stations (Figure 19) and the GI in this case is around 1.2. In this way, we are able to compute the time delays between the perturbation measured by the different stations with respect to *ac*59 (reference station).

Once the time delays are known, we compute the gradient parameters depicted in Figures 20, 21, 22, 23. In Figures 20 and 21, we observe that the ionospheric gradient moves from North to South with a speed of approximately 540 m/s. These oscillations of the speed vector are explained by the changes in the estimation of the position vectors of the IPPs in the local coordinate system (geometrical approximations), which influence greatly the speed determination. The width of the gradient is shown in Figure 23

as the gradient moves with time. The total width of the gradient is approximately 12.5 km when all the stations have seen the gradient completely. In this case, the estimations by the stations *av*01, *av*16 and *av*20 are the same because these stations see the gradient almost at the same time. In the case of the slope, we observe a maximum of 265 mm/km for four of the stations around the time 62402 GPS seconds of day in Figure 22. This local maximum lasts only one second, which could be an effect of the noise and multipath inside the carrier phase measurements when computing the first derivative every second. However, all the stations estimate a slope over 120 mm/km in different points in time, which is a realistic value for the perturbance depicted in Figure 5 (approximately 1.5 meters of change with a total width of 12.5 km).

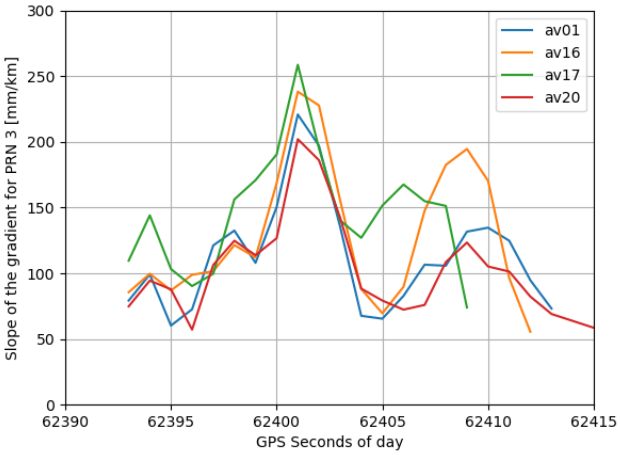

Figure 22: Slope of the gradient (GPS satellite 3, day 76 of year 2015, Alaska).

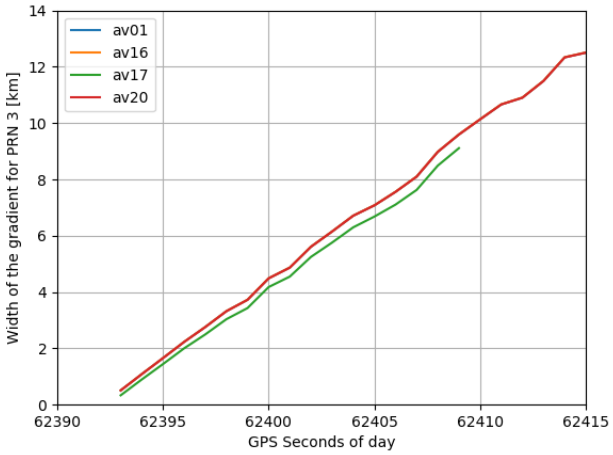

Figure 23: Width of the gradient (GPS satellite 3, day 76 of year 2015, Alaska).

VI. CONCLUSIONS AND FUTURE WORK

In this work, we present a method capable of detecting ionospheric gradients in real-time and estimating their parameters in near real-time, based on a wide area network of dual-frequency and multi-constellation GNSS monitoring stations.

First, we explain the derivation of the detection thresholds for each of the monitoring stations. Here, we make use of a cycle slip detector that searches for cycle slips in the ionospheric-free combination of the carrier phase measurements. In this way, we remove the cycle slips from the measurements, avoiding the inaccurate calculation of the monitoring thresholds.

Then, we describe the methodology during the real-time operation of the algorithm. In this case, the use of the cycle slip detector previously mentioned prevents false alarms. Additionally, we define a geometry index to check if the clusters formed with the IPPs to estimate the gradient parameters are suitable to limit the geometrical approximation errors in the methodology.

Finally, we evaluate our algorithm with simulated gradients and a real gradient measured by a reference network in Alaska. Simulation results show the potential of our algorithm to support GBAS by detecting the gradients and estimating the gradient parameters instead of assuming always the worst-case. Here, the largest errors occur when varying the speed of the gradient. For simulated speeds of the gradient below 400 m/s, there is a predominancy of the errors caused by the noise and multipath effects and for higher speeds, the largest influences are the geometrical aproximations that we assume in order to estimate the gradient parameters. Results evaluating the performance with a real gradient show the need to adapt the algorithm to the characteristics of the ionospheric perturbations in the studied area, especially if they are fast travelling, short duration and fast changing with their propagation. For the gradient studied, this was challeging since keeping an expected value of the cross-correlation above 95% resulted in utilizing only the stations that are very close in distance, which detected the gradients almost at the same times. When adapting the expected maximum value of the cross-correlation to the fast varying nature of the perturbations in the Alaska area, we could use a station further away and therefore obtain promising estimations of the gradient parameters.

Future work will continue developing the methodology further to reduce the impact of carrier phase noise and multipath on the detection and estimation of the gradient parameters and update the simulated gradients to more complex models.

REFERENCES

[1] RTCA-DO-253C,, "Minimum Operational Performance Standards for GPS Local Area Augmentation System Airborne Equipment," *Tech. rep. 253C. Radio Technical Commission for Aeronautics*, vol. 16, 2008.

[2] RTCA-DO-253D,, "Minimum Operational Performance Standards for GPS Local Area Augmentation System Airborne Equipment," *Tech. rep. 253D. Radio Technical Commission for Aeronautics*, 2017.

[3] Datta-Barua, S., Lee, J., Pullen, S., Luo, M., Ene, A., Qiu, D., Zhang, G., and Enge, P., "Ionospheric threat parameterization for local area Global-Positioning-System-based aircraft landing systems," *Journal of Aircraft*, vol. 47, no. 4, pp. 1141–1151, 2010.

[4] Mayer, C., Belabbas, B., Jakowski, N., Meurer, M., and Dunkel, W., "Ionosphere Threat Space Model Assessment for GBAS," *Proceedings of ION GNSS 2009*, 2009.

[5] Yoon, M., Kim, D., and Lee, J., "Validation of Ionospheric Spatial Decorrelation Observed During Equatorial Plasma Bubble Events," *IEEE Transactions on Geoscience and Remote Sensing*, vol. 55, no. 1, pp. 261–271, 2017.

[6] Yoon, M., Kim, D., and Lee, J., "Assessment of Equatorial Plasma Bubble Impacts on Ground-Based Augmentation Systems in the Brazilian Region," in *2016 ION International Technical Meeting (ITM)*, The Institute of Navigation, 2016.

[7] ICAO-NSP3,, "Proposed amendments to annex 10: Ground-based augmentation system (GBAS) provisions," November 2016.

[8] Khanafseh, S., Pullen, S., and Warburton, J., "Carrier phase ionospheric gradient ground monitor for GBAS with experimental validation," *Navigation*, vol. 59, no. 1, pp. 51–60, 2012.

[9] ICAO-NSP,, "Standards and Recommended Practices (SARPs)," *Annex 10, Aeronautical Telecommunications, Volume I*, 2017.

[10] Caamano, M., Gerbeth, D., Felux, M., and Circiu, M.-S., "Using a Wide Area Receiver Network to Support GBAS Ionospheric Monitoring," *Proceedings of ION GNSS+ 2017*, 2017.

[11] Misra, P. and Enge, P., "Global Positioning System: Signals, Measurements and Performance Second Edition," *Massachusetts: Ganga-Jamuna Press*, 2006.

[12] Klobuchar, J. A., "Ionospheric time-delay algorithm for single-frequency GPS users," *IEEE Transactions on aerospace and electronic systems*, no. 3, pp. 325–331, 1987.

[13] Juan, J. M., Sanz, J., Rovira-Garcia, A., González-Casado, G., Ibáñez, D., and Perez, R. O., "AATR an ionospheric activity indicator specifically based on GNSS measurements," *Journal of Space Weather and Space Climate*, vol. 8, p. A14, 2018.

[14] Sanz, J., Juan, J., and Hernández-Pajares, M., "GNSS data processing, Vol. I: fundamentals and algorithms. ESA communications," tech. rep., ESTEC TM-23/1, Noordwijk, Netherlands, 2013.

[15] Juan, J., Aragon-Angel, A., Sanz, J., González-Casado, G., and Rovira-Garcia, A., "A method for scintillation characterization using geodetic receivers operating at 1 Hz," *Journal of Geodesy*, vol. 91, no. 11, pp. 1383–1397, 2017.

[16] Circiu, M.-S., Caizzone, S., Felux, M., Enneking, C., Markus, R., and Meurer, M., "Development of the dual-frequency dual-constellation airborne multipath models," *Navigation: Journal of The Institute of Navigation (under publication)*, 2019.

[17] Xiong, S., "Threshold Determination for Integrity Monitoring in Local Area Augmentation System," in *China Satellite Navigation Conference (CSNC) 2015 Proceedings: Volume II*, pp. 293–300, Springer, 2015.

[18] Hernández-Pajares, M., Juan, J., and Sanz, J., "Medium-scale traveling ionospheric disturbances affecting GPS measurements: Spatial and temporal analysis," *Journal of Geophysical Research: Space Physics*, vol. 111, no. A7, 2006.